

Vibrational Radar Backscatter Communications Theory and Bound

Jessica Centers *Student Member, IEEE* and Jeffrey Krolik *Fellow, IEEE*

Abstract—Vibrational radar backscatter communication (VRBC) utilizes millimeter-wave radar vibrometry to receive message signals from vibrating surfaces. So long as multiple transponding surfaces are separable by the system radar in angle and/or range, VRBC can simultaneously detect, isolate, and decode messages from these multiple sources. For anything-to-vehicle communications, VRBC is therefore a scalable, low-latency approach which leverages existing automotive radars to increase situational awareness without requiring any additional use of the RF spectrum. In this paper, we describe the modeling and processing of VRBC signals. We show that knowledge of surface resonances and coding constraints can be used to improve system performance by incorporating them into a Markov model. We provide insight into the rate capabilities of VRBC by providing a theoretical upper bound that incorporates the presence of intersymbol interference (ISI). Simulation results compare our upper bound to achievable communication rates using single symbol vs sequence detection maximum likelihood methods for a given symbol length, set of symbol excitations, and VRBC radar pulse repetition interval (PRI).

Index Terms—millimeter-wave radar, backscatter communication, vibrometry, channel rate bound

I. INTRODUCTION

MODULATING backscatter has served as a low-cost communication solution since Stockman introduced the concept in 1948 [1]. As exemplified by standard radio frequency identification (RFID), backscatter communication typically operates at UHF frequencies due to this band's efficient backscatter characteristics [2]–[4]. To achieve adequate signal returns, backscatter communication at millimeter (mmW) frequencies, however, requires complex and expensive retro-directive antennas or miniaturized high-gain antenna arrays [5]–[7].

Recently, we introduced the concept of vibrational radar backscatter communications (VRBC) which uses a mmW automotive radar to perform a new form of backscatter communication [8]. In contrast to traditional backscatter communication systems, VRBC uses the radar as a vibrometer, thus avoiding the challenge of requiring a matched antenna that also has a radar cross section (RCS) that provides adequate backscatter strength. Instead of the backscatter modulation appearing as a change in amplitude due to a change in transponder impedance, VRBC modulation comes in the form of phase modulation caused by changes in a vibrating surface's displacement. The vibrational transponder itself can be as

simple as a loudspeaker, like we used in [8], or a more optimally designed active transponder with a controllable surface displacement. Regardless, the modulation appears primarily in the backscatter's slow-time phase when the radar's waveform is that of a traditional frequency modulated continuous wave (FMCW) radar.

Vibrometry at mmW has been used in other applications such as structural analysis [9], acoustic signal reconstruction [10], wireless communication across medium boundaries [11], search and rescue operation [12], and voice authentication [13]. With the autonomous vehicle industry advancing mmW radar technology and making their installation in modern vehicles commonplace, anything-to-vehicle communication naturally fits as an additional application space for mmW vibrometry as it offers a way to increase vehicle situational awareness while requiring minimal additional infrastructure.

Communication to and from vehicles has historically required either sharing resources with radar systems or optimizing waveforms that can be used for both sensing and communications. The former method, often described as the cohabitation of radar and communication systems, typically requires cooperative sensing techniques to reactively mitigate mutual interference [14]–[16]. A novel radar estimation information rate was described in [17] to help quantify how to balance power between the two operations. Alternatively, joint radar and communication co-design waveforms allow a single active RF emission to act as the radar waveform while also containing modulation for a communication signal [18], [19]. Solutions of this nature tend to include waveform designs that inherit primary characteristics from one of the two systems' traditional waveforms. Of particular interest in applications such as connected vehicles are radar waveform-based designs where communication functions are integrated into an existing radar system by modifying the waveform to include digitally modulated data symbols [20], [21]. Both cohabitation and co-design solutions demonstrate some amount of tradeoff between sensing and communication performance capabilities. Because VRBC allows messages to exist within the phase of backscatter, it provides a way in which sensing and communications can be done simultaneously with no modification to the standard radar waveform being used.

VRBC provides the additional benefit of offering numerous communication channels. Traditional anything-to-vehicle communication methods have a limited number of channels constrained by the system's total bandwidth. In VRBC, the number of communication channels available to a particular vehicle scales with the range and bearing resolution of the automotive radar, as illustrated in Fig. 1. Accordingly, VRBC

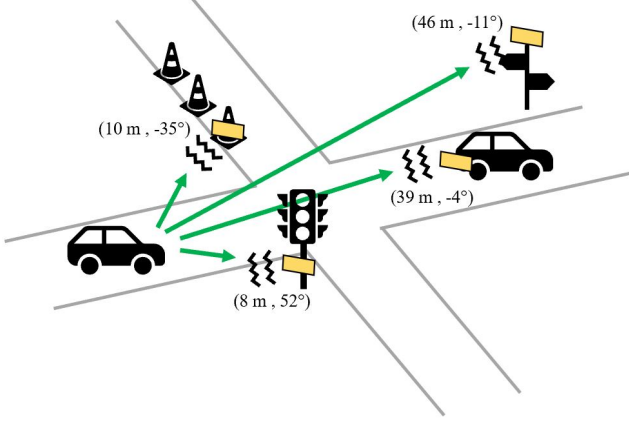


Fig. 1. An anything-to-vehicle scenario demonstrating the simultaneous multichannel signal reception of VRBC to the mmW radar-equipped left-most vehicle. The green arrows indicate paths along which the radar signal travels and reflects from targets back to the on-vehicle radar. Vibrational transponding surfaces are in yellow and characteristic yet arbitrary bearing angles and ranges in relation to the receiving vehicle.

could serve as a beneficial add-on particularly in high traffic scenarios to alleviate network congestion for line-of-sight anything-to-vehicle communication [22].

In this paper, we provide the theory behind VRBC, which includes a processing chain to describe how communication signals can be detected and decoded from the system's received backscatter signal. Though we avoid claiming truly optimal detection, since techniques which e.g. exploit multipath [23] could further improve system performance, we do implement both single symbol and sequence maximum likelihood detection methods in message decoding. Discussion surrounding when one message detection method should be used over the other is provided, and the achieved communication rates using both methods is compared to an analytical upper bound.

Throughout this paper, we refer to the vibrational surfaces that contain message signals as targets as well as transponders even though they are not required to be moving with a bulk velocity, as is characteristic of traditional radar targets, nor do they actively emit RF waves. We adopt notation in which all vectors are bolded and lowercase, matrices are bolded and uppercase, and sets are in calligraphy. Vectors are assumed to be column vectors unless otherwise stated. We use $\mathbb{E}[\cdot]$ and $\Pr(\cdot)$ to indicate an expectation and a probability respectively. All other notation is identified as it appears.

We begin by showing how a vibrational displacement message signal in VRBC appears in the return of an FMCW radar in Section II. Section III demonstrates how the full return fits into a Markov model framework. A useful analytical upper bound on data rate is then calculated in Section IV. This bound is then compared to simulated rate results in Section V. A brief conclusion is offered in Section VI.

II. RADAR MODEL AND SIGNAL PROCESSING

To observe how a VRBC message-bearing surface displacement appears in an FMCW radar's return, we begin by defining

the transmitted FMCW radar waveform as

$$s_{\text{TX}}(t) = \alpha_{\text{TX}} e^{j2\pi f_0 t} \sum_{g=0}^{G-1} u_p(t - gT_{\text{PRI}} - t_0), \quad (1)$$

where α_{TX} is the gain/attenuation associated with the transmitter, f_0 is the start frequency of the chirps, G is the number of chirps sent, T_{PRI} is the pulse repetition interval, t_0 is the start time of the whole signal, and $u_p(t)$ is the FMCW baseband waveform. We define

$$u_p(t) = \begin{cases} e^{j\pi\beta t^2} & 0 \leq t < T \\ 0 & \text{otherwise} \end{cases}, \quad (2)$$

where T is the active duration of a chirp which must be less than or equal to T_{PRI} . The chirp slope is $\beta = \frac{B}{T}$ and B is the bandwidth of the chirp.

Only the return containing the target is desired for the purposes of VRBC, so we continue under the assumption that the full return is only from the beam in the direction of the target. When a beam output contains only a single vibrating target transponder, the received signal consists of the backscatter of the transmitted signal from the vibrating transponder, $s_{\text{RX}_{\text{tar}}}(t)$; clutter, $s_{\text{RX}_{\text{clt}}}(t)$; and additive white Gaussian noise (AWGN), $\tilde{n}(t)$;

$$s_{\text{RX}}(t) = s_{\text{RX}_{\text{tar}}}(t) + s_{\text{RX}_{\text{clt}}}(t) + \tilde{n}(t). \quad (3)$$

Without loss of generality, assume the start time, t_0 , is 0. The return from the target is modeled as a flat fading surface

$$s_{\text{RX}_{\text{tar}}}(t) = \tilde{\alpha}_{\text{tar}} e^{j2\pi f_0 (t - \tau_{\text{tar}}(t))} \sum_{g=0}^{G-1} u_p(t - \tau_{\text{tar}}(t) - gT_{\text{PRI}}), \quad (4)$$

where $\tau_{\text{tar}}(t)$ is the round trip delay observed due to the range from the radar to the target. This models the cases of a retro-directive reflectors and/or surface backscatter with roughness much less than the range resolution of the radar. In the anything-to-vehicle communication scenario, the former case is exemplified when the transponder is a traffic sign or license plate at ranges greater than a few meters.

If we assume the radar and target move at some bulk velocity such as when the radar is on a moving vehicle or the vibrational surface is mounted on another moving vehicle, we can write the delay as

$$\tau_{\text{tar}}(t) = \frac{2}{c} (r_{\text{tar}} + v_{\text{tar}}t - v_{\text{radar}}t + d(t)). \quad (5)$$

The term r_{tar} is the initial range between the transponder target and VRBC radar, v_{tar} is the radial velocity of the target, v_{radar} is the radial velocity of the radar, and $d(t)$ is the transponder's radial surface displacement. Here, we assume radar-facing surfaces so that that object's radial displacement is significant. A more retro-directive transponder is desirable and poses an interesting area of future research. This paper, however, does not require a specific transponder design and only assumes a system in which adequate radial surface displacement is present. Equation 5 has also been written assuming that positive radial velocities are in the forward direction from the perspective of the radar.

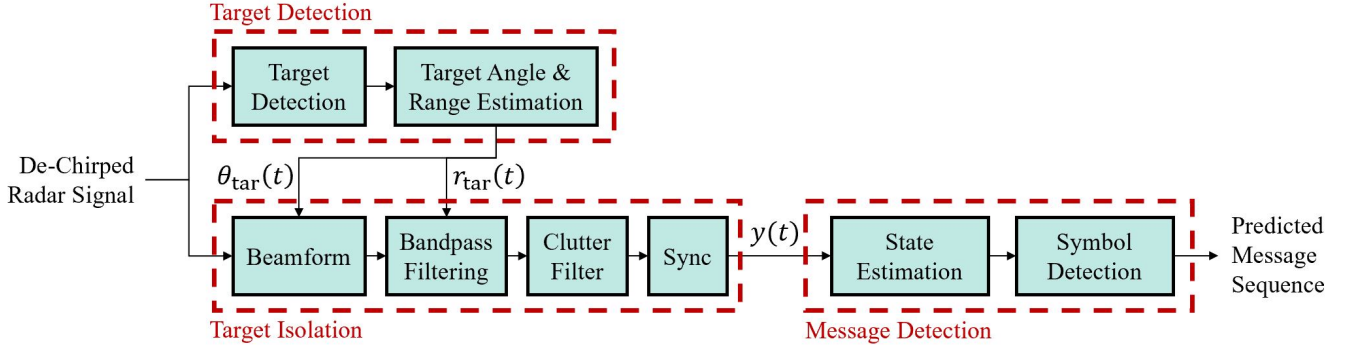


Fig. 2. The processing chain used to get the message signal in a VRBC system.

In Equation 4, $\tilde{\alpha}_{\text{tar}}$ is the amplitude after scaling due to signal propagation as a function of the target's range and radar cross section (RCS). The tilde indicates that this term is complex. Specifically, all $\tilde{\alpha}$ terms going forward are complex Gaussian random variables following the Swerling model [24]. Details of the statistical characteristics of these terms can be found in Appendix A.

The target-directed clutter return within a beam can be modeled as a sum of K point scatterers

$$s_{\text{RX}_{\text{clt}}}(t) = \sum_{k=1}^K \tilde{\alpha}_k e^{j2\pi f_0(t-\tau_k(t))} \sum_{g=0}^{G-1} u_p(t - \tau_k(t) - gT_{\text{PRI}}). \quad (6)$$

Each clutter point indexed by k has delay

$$\tau_k(t) = \frac{2}{c}(r_k - v_{\text{radar},k}t), \quad (7)$$

where r_k is the range of the k^{th} clutter point, while $v_{\text{radar},k}$ is the radial velocity of the radar with respect to the k^{th} clutter point. The radial velocity relates to the absolute velocity and azimuthal angle θ_k measured from the direct of motion of the point via $v_{\text{radar},k} = v_{\text{radar},k}^{(\text{abs})} \cos \theta_k$. Because this return contains clutter points from the full beam, there exists multiple clutter points for which their ranges are equal but their complex amplitudes and radial velocities for the radar differ. This subset of points represents the clutter along the arc that spans the beamwidth of the radar at a particular range. The Doppler spread due to the radar's absolute motion can then be calculated using

$$\Delta f_D = \frac{2}{\lambda_0} v_{\text{radar}}^{(\text{abs})} \Delta \cos \theta_k, \quad (8)$$

where $\Delta \cos \theta_k$ denotes the difference in $\cos \theta$ due to the edge points of the beamwidth of the radar.

Following conventional FMCW processing methods, the entire beam return, Equation 3, is first de-chirped by multiplying the received signal by the complex conjugate of the

transmitted,

$$s_{\text{TX}}(t)s_{\text{RX}}^*(t) = \tilde{\alpha}_{\text{tar}} e^{j2\pi f_0 \tau_{\text{tar}}(t)} \sum_{g=0}^{G-1} z_{\text{tar}}(t - gT_{\text{PRI}}) + \sum_{k=1}^K \tilde{\alpha}_k e^{j2\pi f_0 \tau_k(t)} \sum_{g=0}^{G-1} z_k(t - gT_{\text{PRI}}) + \tilde{n}(t) \quad (9)$$

where

$$z_{\text{obj}}(t) = \begin{cases} e^{j\pi\beta(2\tau_{\text{obj}}(t)t - \tau_{\text{obj}}^2(t))} & \tau_{\text{obj}}(t) \leq t < T \\ 0 & \text{otherwise} \end{cases} \quad (10)$$

In radar processing, $\tau_{\text{obj}}(t)$ is typically considered constant within a chirp, ie. not a function of time within $z_{\text{obj}}(t)$. In such cases, this simplifies $z_{\text{obj}}(t)$ to a complex sinusoid with a frequency proportional to range. This is an assumption that VRBC cannot always make however, due to the frequencies of vibration being similar to the radar's PRF. For that reason, we continue with the generalized representation. In reference to our full processing chain shown in Fig. 2, Equation 9 is the output of the beamforming block in the target isolation sequence for an arbitrary transponder.

To reach Equation 9, target detection must first be completed. Target detection is not the focus of this paper, but would consist of using constant false alarm rate (CFAR) detection to find VRBC transponders in range-bearing space. This method would detect objects in the scene that are not being used for VRBC as well. To ensure that only vibrating transponders are decoded through the remainder of the VRBC processing chain, the Doppler of all detected objects would need to be analyzed to determine whether they consist of displacements at frequencies specific to VRBC. Parameter estimation of each transponder's angle and range would be then calculated.

The processing sub-chain labeled as target isolation, then separates targets within a single beam at different ranges. It is important to distinguish that VRBC range processing differs from traditional techniques. Traditional FMCW range processing consists of organizing the signal into a matrix of fast- and slow-time samples, or samples within chirp versus samples across chirps. Usually an FFT is taken in fast-time to provide a matrix of range versus slow-time samples. This allows range processing to simply be the act of keeping only the slow-time vector associated with the range desired.

Because VRBC vibrations lead to Doppler movements that are not constant or insignificant within a chirp, we instead bandpass filter the full de-chirped beam return in order to separate signals in range. This leaves the signal in the traditionally labeled fast-time domain. The significance of this variation in processing is visualized in Fig. 3, where we can clearly observe energy due to a target's displacement existing at sub-bands outside of the one most closely associated with the range of the target. Bandpass filtering also causes the AWGN term to become band-limited. We denote band-limited noise as $\tilde{\eta}(t)$.

For each individual transponder detected and isolated, clutter filtering and independent synchronization is conducted. Typically, clutter filtering is done in the slow-time domain. Since our model keeps the signal in fast-time, this would mathematically appear as

$$y(t) = \sum_{n=0}^N w_n s_{\text{TX}}(t + nT_{\text{PRI}}) s_{\text{RX}}^*(t + nT_{\text{PRI}}). \quad (11)$$

Here, N is the order of the filter and w_n is the filter coefficient for the n^{th} tap. When clutter is stationary relative to the radar (ie. $v_{\text{radar}} = 0$), the only non-zero filter coefficients can be $w_0 = 1$ and $w_1 = -1$. In other words, because stationary clutter is consistent across chirps, clutter filtering results in subtracting off the previous chirp to mitigate the portion of the return that is consistent. The frequency response of such a filter would appear as a series of notches at multiples of the PRF. Figure 3 shows the spectra of a sample VRBC channel both before and after clutter filtering in this manner. In practice, it is possible that clutter could be non-stationary. Take for example when $v_{\text{radar}} \neq 0$ or clutter consists of leaves from a nearby tree moving in the wind. In these cases, filter weights will be less trivial and methods to estimate the filter weights such as using space-time adaptive processing techniques would be required [25].

After clutter filtering, synchronization must occur to find the start of a VRBC message sequence. This is done for each transponder signal individually. To achieve synchronization, a known preamble sequence with an autocorrelation function that results in a sharp peak is used in all vibrational message signals. The time index associated with a peak in the correlation between a VRBC signal and known preamble would then provide the sequence start time.

Upon synchronization, the radar model for VRBC return is now given as

$$y(t) = y_{\text{tar}}(t) + \tilde{\eta}(t) \quad (12)$$

where

$$y_{\text{tar}}(t) = \tilde{\alpha}_{\text{tar}} \sum_{n=0}^N w_n e^{j2\pi f_0 \tau_{\text{tar}}(t+nT_{\text{PRI}})} \sum_{g=-n}^{G-1-n} z_{\text{tar}}(t - gT_{\text{PRI}}).$$

Recall that the message-encoded displacement $d(t)$ appears within the delay $\tau_{\text{tar}}(t + nT_{\text{PRI}})$ using Equation 5.

The displacement of a VRBC surface, $d(t)$, can be written as a function of an excitation signal causing the vibrations, $x(t)$. The excitation signal is equivalently the encoded mes-

sage signal. Consider an excitation signal that consists of Q consecutive single symbol excitations,

$$x(t) = \sum_{q=1}^Q x_q(t - (q-1)T_{\text{sym}}) \quad (13)$$

where each $x_q(t) \in \mathcal{X}$. The set \mathcal{X} contains M different symbol excitations that have non-zero values only from $0 \leq t < T_{\text{sym}}$, $\mathcal{X} = \{x^{(1)}(t), x^{(2)}(t), \dots, x^{(M)}(t)\}$. The excitation length is the same for all M possible symbols and is notated as T_{sym} seconds or L_{sym} samples long, where $L_{\text{sym}} = T_{\text{sym}} f_s$. Here, the sampling frequency, f_s , is the de-chirped radar signal sampling frequency. For simplicity, we assume that the symbol length is a positive integer multiple of the pulse repetition interval (PRI).

By modeling the vibrating surface as a linear time-invariant system, the vibrational displacement is

$$d(t) = \sum_{q=1}^Q d_q(t - (q-1)T_{\text{sym}}) \quad (14)$$

where

$$d_q(t) = \sum_{n=0}^{q-1} x_{q-n}(t - nT_{\text{sym}}) \otimes h(t) \quad (15)$$

for $0 \leq t < T_{\text{sym}}$ and 0 otherwise. The symbol \otimes is the convolution operation and $h(t)$ is the surface's impulse response. In practice, an accurate estimate of $h(t)$ is needed to use the maximum likelihood detection methods we describe in this paper. We describe the set of possible displacements for a single symbol interval as $\mathcal{D} = \{d^{(1)}(t), d^{(2)}(t), \dots, d^{(D)}(t)\}$. Note that $D \neq M$ if the convolution resulting in displacement leads to different displacements during intervals of the same excitation symbol due to previous symbol contributions.

By substituting Equation 14 into 5 which is then used in 12, the VRBC channel can be described by the excitation/message for a given transponder range and trajectory (r_{tar} , v_{tar} , and v_{radar}). To highlight that the target-derived component of the signal $y_{\text{tar}}(t)$ is a function of $d(t)$, we write

$$y(t) = \sum_{q=1}^Q y_q(t - (q-1)T_{\text{sym}}) \quad (16)$$

where

$$y_q(t) = y_{q,\text{tar}}(d_q(t)) + \tilde{\eta}(t) \quad (17)$$

and $y_{q,\text{tar}}(d_q(t)) = y_{\text{tar}}(t)$ for $(q-1)0 \leq t < qT_{\text{sym}}$ and 0 elsewhere. The target-derived component, $y_{q,\text{tar}}(t)$ takes on a finite number of realizations described by the set $\mathcal{Y}_q = \{y_{q,\text{tar}}^{(1)}(t), y_{q,\text{tar}}^{(2)}(t), \dots, y_{q,\text{tar}}^{(D)}(t)\}$, which directly relate to the displacement of the VRBC transponder, $y_{q,\text{tar}}^{(d)}(t) = y_{\text{tar}}(t)$ given $d(t) = d^{(D)}(t)$. The set \mathcal{Y}_q does differ per symbol interval q , if the target is moving relative to the radar. The cardinality of the set for all q remains constant, however, due to the number of possible displacements being unaffected by relative transponder motion. If the transponder is not moving relative to the radar, then \mathcal{Y}_q is the same for all q .

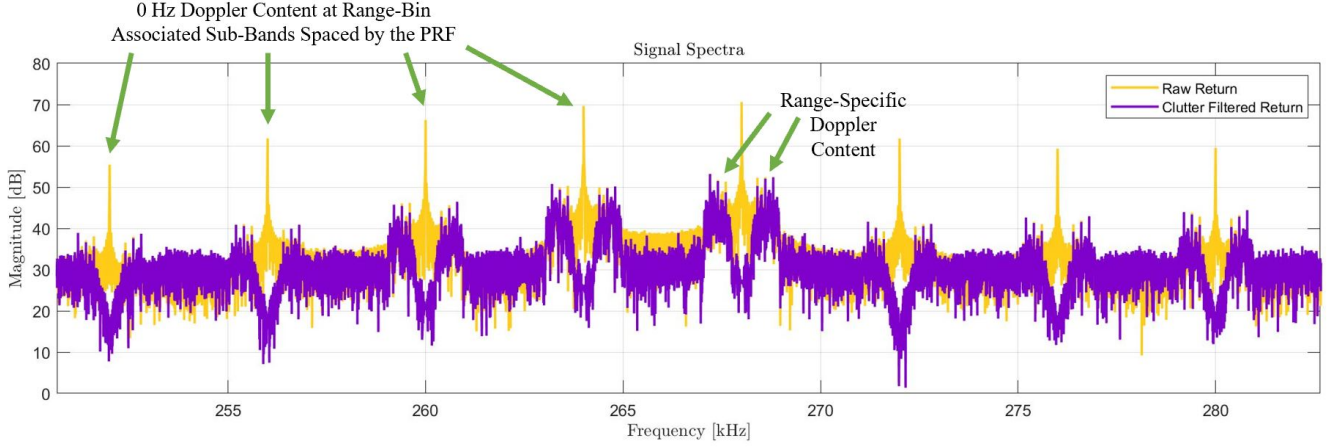


Fig. 3. The spectra of a sample VRBC channel return. An assumed fully reflective aluminum license plate-sized transponder was simulated at ~ 30 dB target power. The message signal simulated was a 100-symbol long, M -ary FSK sequence of vibrations at 800, 600, and 400 Hz.

III. COMMUNICATION MESSAGE MODEL AND DETECTION

In sets \mathcal{D} and \mathcal{Y}_q , their cardinality D once again refers to the number of possible displacements and possible target-derived signal components. These sets are generated by considering the transponder's range, trajectory, and impulse response to be known parameters that appear in our model as described in Section II. In this paper, we assume these parameters are estimated well using traditional range and tracking techniques and a system identification method for impulse response estimation. The task of putting the return into a Markov model, therefore, primarily consists of accounting for surface resonant effects and message coding constraints. To do so, we first consider symbol to symbol dependencies of a VRBC transponder.

Any real vibrational surface has a nontrivial, causal, and stable impulse response $h(t)$. Previous symbol excitations will therefore contribute to the displacement observed during a given symbol interval, $(q-1)T_{\text{sym}} \leq t < qT_{\text{sym}}$ for symbol index $q \geq 0$. This undesirable characteristic results in intersymbol interference (ISI). In mitigating ISI, it is common to make use of line coding constraints that avoid error-prone patterns from occurring in a message sequence. Both ISI and coding constraints present themselves in the form of previous symbol interval dependencies from the perspective of the current symbol interval. Though it results in ISI, resonant surfaces can be favorable in that they often lead to larger maximum displacements, which puts more of the power due to vibrations existing at frequencies outside of 0 Hz Doppler. This relationship is explained further in [8].

In general, the observed vibrational displacement for the q^{th} symbol interval can be estimated using the interference from a finite number of previous symbols rather than all the previous symbols as described in Equation 15. Let

$$d_q(t) = \sum_{n=0}^{N_q} x_{q-n}(t - nT_{\text{sym}}) \otimes h(t) \quad (18)$$

for $0 \leq t < T_{\text{sym}}$ and 0 otherwise. Here, N_q is the number of symbols previous whose vibrational transients interfere with

the current symbol's vibrational displacement. This model assumes that for the q^{th} symbol interval that all vibrations due to symbols prior to the $(q - N_q)^{\text{th}}$ symbol have decayed to a negligible amount.

Picking N_q is not required to be done in a particular way, but it does always require considering the full resonant displacements of each symbol excitation, $x^{(m)}(t) \otimes h(t)$, and implementing some constraint on what defines a negligible amount of displacement. In this paper, we define a negligible amount of interfering displacement as displacement with a magnitude less than a chosen ratio of the maximum absolute displacement provided by any of the M symbol excitations. We call this ratio γ_{\min} . We allow γ_{\min} to dictate a different number of symbol intervals for which it takes each of the M symbol excitations to decay out to the negligible amount. The set \mathcal{N} is used to describe the system's symbol-specific resonances, $\mathcal{N} = \{N^{(1)}, N^{(2)}, \dots, N^{(M)}\}$, where element $N^{(m)}$ describes the number of symbol intervals it takes the m^{th} symbol to decay to $\gamma_{\min} \max_{t,m}(d^{(m)}(t))$.

The choice in γ_{\min} does affect detection performance. If γ_{\min} is too large, then detection performance degrades as the interference present becomes inaccurately represented. Alternatively, choosing a smaller γ_{\min} will create a more accurate representation but will also increase the model complexity and eventually provide no additional performance benefits in sequence detection over single symbol detection.

In a Markov model, states and transition events are used to describe how a sequence of observations depend on previous observations. In VRBC, ISI and coding constraints dictate the possible observations a given symbol interval can have. Let

$$d_q(t) - (x_q(t) \otimes h(t)) \in \mathcal{D}_{\text{ISI}}. \quad (19)$$

define the ISI of the q^{th} symbol interval where \mathcal{D}_{ISI} is the set of possible ISI displacements and has a cardinality we denote as S to stand for the number of VRBC states. The set of possible ISI conditions/states can be found by considering all symbol sequence permutations of the M symbols of length $\max(\mathcal{N})$ or less. Coding constraints and a non-uniform \mathcal{N} can lead

to certain permutations being unachievable or unnecessary to define distinctly.

We now argue that $y_q(t)$ is independent of $y_{q-i}(t)$ given $y_{q-1}(t)$ for $i > 1$ since no interval's displacement can be dependent on more than the previous when the previous is defined on ISI that is only further decaying out and remaining negligible in the current interval. Transition events for a VRBC Markov model are then described by the symbol excitation of the current interval as it is these new symbols that define what the ISI will look like in the next symbol interval, ie. what state we must transition to.

It is insufficient to describe states and transition events alone. Their transition probabilities must also be fully described in order for detection to benefit from this model. Transition probabilities are found using knowledge of our state definitions and any line coding constraints. Examples will be shown to further demonstrate how this is done exactly, but once defined, we describe them in a state transition matrix \mathbf{A} , within which element $A_{i,j}$ describes the probability of transitioning from state i to state j .

Using the notation that m_q and s_q are the q^{th} symbol and state in a VRBC sequence where $m_q \in 1, 2, \dots, M$ and $s_q \in 1, 2, \dots, S$, we summarize the Markov model description as:

- states: defined by the ISI present within a symbol interval
- transition event: defined by any new symbol in a sequence
- Markov property: $\Pr(s_q | s_1, s_2, \dots, s_{q-1}) = \Pr(s_q | s_{q-1})$
- transition matrix: $A_{i,j} = \Pr(s_q = j | s_{q-1} = i)$

Example 1. Non-Resonant Surface Case: Consider $M = 3$ excitation symbols chosen such that ISI is eliminated. One way in which the no-ISI case could be realized is by designing each symbol to have non-zero excitation for some smaller fraction of the full symbol length. This would allow the vibrational surface to return to equilibrium before the next symbol interval begins. Therefore $\mathcal{N} = \{0, 0, \dots, 0\}$ and the displacement for a single symbol interval reduces to

$$d_q(t) = x_q(t) \otimes h(t), \text{ for } 0 \leq t < T_{\text{sym}}. \quad (20)$$

In this example, we assume that no line coding is used as it would serve no purpose since there is no ISI. This scenario would therefore result in a single state

TABLE I
STATES FOR $M = 3$ AND $\mathcal{N} = \{0, 0, 0\}$

State Index	Sequences
1	—

The “—” symbol notation is used to indicate a symbol interval in which the excitation at this interval does not contribute to the current symbol interval's displacement.

Because there is no line coding, we construct the transition matrix assuming equiprobable symbols. For this example, the transition matrix is simply $\mathbf{A} = [1]$.

Example 2. Resonant Surface Case: Now consider an alternative $M = 3$ case. In this example, assume that all symbols produce non-negligible amounts of ISI for at least one symbol interval, $\min(\mathcal{N}) \geq 1$. Specifically, we use $\mathcal{N} = \{2, 1, 1\}$.

Consequently, we also adopt a simple coding constraint in which consecutive symbols are not possible, $m_q \neq m_{q-1}$, as to attempt to mitigate the errors caused by previous symbol ISI. Furthermore, consider any symbol interval to have equally probable chances of being any of the M symbols besides for whatever the previous symbol was, $\Pr(m_q = m) = \frac{1}{M-1}$ for all $m \neq m_{q-1}$.

TABLE II
STATES FOR $M = 3$ AND $\mathcal{N} = \{2, 1, 1\}$

State Index	Sequences
1	— —
2	— 1
3	— 2
4	— 3
5	1 1
6	1 2
	1 3
	2 1 \rightarrow — 1
	2 2 \rightarrow — 2
	2 3 \rightarrow — 3
	3 1 \rightarrow — 1
	3 2 \rightarrow — 2
	3 3 \rightarrow — 3

When no coding scheme is invoked, the possible states are described by the full list of possible sequences of the M symbols that are of length $\max(\mathcal{N})$ or less. These sequences are described in the rows of Table II. The sequences in the table are formatted such that reading the symbol sequences left to right goes from the most previous contributing symbol interval's excitation to the most recent symbol interval's excitation, i.e. the $(q - \max(\mathcal{N}))^{\text{th}}$ to the $(q - 1)^{\text{th}}$ symbol interval.

After all possible states are generated, instances in which symbol excitations would no longer contribute ISI to the current symbol interval's displacement were replaced with the no-contribution symbol, often leading to duplicates of an existing state allowing for a state elimination. This replacement is shown via the “ \rightarrow ” in Table II. For example the sequences of “2 1” became “— 1” because $N^{(2)} = 1$ and therefore would not contribute ISI in the $q - 2^{\text{th}}$ position. Lastly, using our basic coding scheme of avoiding consecutive symbols requires that states violating this constraint be eliminated. The sequence of “1 1” exemplifies this. The states that remain in the $M = 3$ and $\mathcal{N} = \{2, 1, 1\}$ example are those indexed in Table II.

For this example, the transition matrix is

$$\mathbf{A} = \begin{bmatrix} 0 & \frac{1}{3} & \frac{1}{3} & \frac{1}{3} & 0 & 0 \\ 0 & 0 & 0 & 0 & \frac{1}{2} & \frac{1}{2} \\ 0 & \frac{1}{2} & 0 & \frac{1}{2} & 0 & 0 \\ 0 & \frac{1}{2} & \frac{1}{2} & 0 & 0 & 0 \\ 0 & \frac{1}{2} & 0 & \frac{1}{2} & 0 & 0 \\ 0 & \frac{1}{2} & \frac{1}{2} & 0 & 0 & 0 \end{bmatrix} \quad (21)$$

when a coding scheme constraining consecutive symbols is implemented and all remaining symbols are equiprobable. As this matrix shows, the beginning state of no-ISI is unachievable at any point in the sequence besides for the start since this example assumed all symbols produce non-negligible amounts of ISI for at least on symbol interval. We also see that states 5 and 6 are the only two that require considering more than

the previous symbol in the sequence and can only be reached via a state where '1' was the previous symbol, ie. state 2.

Once put into a Markov model, VRBC detection can be completed using either single symbol or sequence maximum likelihood detection methods. At a top level, VRBC has the following progression from symbol input to symbol prediction,

$$\begin{array}{ccccc} \text{Input Symbol} & \xrightarrow{\text{Channel}} & \text{Output Signal} & \xrightarrow{\text{Detection}} & \text{Predicted Symbol} \\ m_q & & \mathbf{y}_q & & \hat{m}_q \end{array} \quad (22)$$

where predicted symbols are denoted as \hat{m} . Similarly, \hat{s} will denote predicted states moving forward. We also now put the components of the symbol interval return signals $y_q(t)$ into vector form. We use \mathbf{y}_q to denote the full $L_{\text{sym}} \times 1$ column vector of signal samples from the q^{th} symbol interval, \mathbf{a}_q to denote the target-derived component, and $\boldsymbol{\eta}_q$ contains the band-limited AWGN samples,

$$\mathbf{y}_q = \mathbf{a}_q + \boldsymbol{\eta}_q. \quad (23)$$

Let the possible target-derived data vectors be specified using the notation $\mathbf{a}^{(s,m)}$, indicating it results from ISI displacement associated with state s and current symbol displacement associated with the m^{th} symbol.

Single symbol maximum likelihood detection in AWGN is performed using

$$\hat{m}_q = \arg \max_m \Pr(m_q = m) e^{-(\mathbf{y}_q - \mathbf{a}^{(\hat{s}_q, m)})^H \Gamma^{-1} (\mathbf{y}_q - \mathbf{a}^{(\hat{s}_q, m)})} \quad (24)$$

where Γ is the noise covariance matrix. To perform sequence estimation, which we do via the Viterbi algorithm, we define the posterior probabilities, $\Pr(s_q = s | \mathbf{y}_q)$ using Bayes' theorem,

$$\begin{aligned} \Pr(s_q = s | \mathbf{y}_q) &= \frac{f(\mathbf{y}_q | s_q = s) \Pr(s_q = s)}{f(\mathbf{y}_q)} \\ &= \frac{l_s(\mathbf{y}_q)}{\sum_{t=1}^S l_t(\mathbf{y}_q)}, \end{aligned} \quad (25)$$

where

$$l_s(\mathbf{y}_q) = \sum_{m \in \mathcal{M}^{(s)}} \frac{\Pr(s_q = s)}{|\mathcal{M}^{(s)}|} e^{-(\mathbf{y}_q - \mathbf{a}^{(s,m)})^H \Gamma^{-1} (\mathbf{y}_q - \mathbf{a}^{(s,m)})}, \quad (26)$$

and $\mathcal{M}^{(s)}$ is the set of possible current symbols that can occur when in state s .

Equation 25 is found by acknowledging that given a particular state, the output vector has a complex multivariate Gaussian mixture probability density function of,

$$f(\mathbf{y}_q | s_q = s) = \sum_{m \in \mathcal{M}^{(s)}} \frac{1}{|\mathcal{M}^{(s)}|} \tilde{\mathcal{N}}(\mathbf{a}^{(s,m)}, \Gamma) \quad (27)$$

for a single channel use. If the input state is not known, the distribution of the output data vector is the weighted sum of those state-conditioned densities,

$$f(\mathbf{y}_q) = \sum_{s=1}^S \Pr(s_q = s) f(\mathbf{y}_q | s_q = s). \quad (28)$$

The probability of being in a state during a particular symbol interval, $\Pr(s_q = s)$, is found recursively using the the state transition matrix,

$$\boldsymbol{\pi}_q = \boldsymbol{\pi}_{q-1} \mathbf{A}, \quad (29)$$

where $\boldsymbol{\pi}_q$ is the column vector describing the probabilities of each state occurring at the q^{th} symbol interval, ie. $\boldsymbol{\pi}_q = [\Pr(s_q = 1), \Pr(s_q = 2), \dots, \Pr(s_q = S)]^T$. Naturally, $\boldsymbol{\pi}_0 = [1, 0, 0, \dots, 0]^T$ in all cases assuming the first state is always defined as the state where no previous or current symbol excitations contribute to displacement.

In carrying out the Viterbi algorithm, two matrices are calculated for each symbol interval and state combination. These calculations fully describe the standard Viterbi trellis. Define the $S \times Q$ matrices

$$T_1[s, q] = \max_t (T_1[t, q-1] A_{t,s} \Pr(s_q = s | \mathbf{y}_q)) \quad (30)$$

and

$$T_2[s, q] = \arg \max_t (T_1[t, q-1] A_{t,s} \Pr(s_q = s | \mathbf{y}_q)). \quad (31)$$

T_1 tracks the probability associated with the most likely path leading to the the current symbol interval's state being state s . T_2 tracks the previous symbol interval's state prediction associated with the most likely path leading to the current symbol interval's state being state s .

To decide the final sequence observed, the last state detected is found by considering $\arg \max_t (T_1[t, Q])$. Once the sequence of states is found by recursively considering $\hat{s}_q = T_2[\hat{s}_{q+1}, q+1]$, the predicted symbol sequence can easily be found by considering what transition events led (or could have led) to the sequence of predicted states. The phrase "could have led" alludes to the case where $\min(\mathcal{N}) < 1$. In these cases, single symbol maximum likelihood detection is needed to decide between multiple potential transition events. This is most easily understood by observing that sequence detection for the non-resonant surface example we provided would result in a predicted state sequence that is trivial and yields no information on symbol detection. In this specific case, single symbol detection is used to decide between all M symbols, though cases where only some values in $\mathcal{N} < 1$ will benefit from using sequence detection followed by single symbol detection when non-unique state transitions occur.

Once the predicted symbol sequence is found, an estimate of the achieved rate is calculable using the errors between the true and predicted symbol sequences, $\mathbf{m} = [m_1, m_2, \dots, m_Q]^T$ and $\hat{\mathbf{m}} = [\hat{m}_1, \hat{m}_2, \dots, \hat{m}_Q]^T$. The observed mutual information rate is given by

$$\mathbf{R}_{\text{obs}} = \frac{H(\hat{m}_q) - H(\hat{m}_q | m_q)}{T_{\text{sym}}}, \quad (32)$$

where $H(\cdot)$ indicates entropy. Consider a confusion matrix, \mathbf{C} , describing the errors observed. $C_{m,n}$ describes the number of times the m^{th} symbol was predicted to be the n^{th} symbol. Components of Equation 32 are then

$$H(\hat{m}_q) = - \sum_n \left(\frac{\sum_m C_{m,n}}{Q} \right) \log_2 \left(\frac{\sum_m C_{m,n}}{Q} \right) \quad (33)$$

and

$$H(\hat{m}_q|m_q) = \sum_m \left(\frac{\sum_n C_{m,n}}{Q} \right) H(\hat{m}_q|m_q = m), \quad (34)$$

where

$$H(\hat{m}_q|m_q = m) = - \sum_n \left(\frac{C_{m,n}}{\sum_n C_{m,n}} \right) \log_2 \left(\frac{C_{m,n}}{\sum_n C_{m,n}} \right). \quad (35)$$

Using our knowledge of the symbol vector distributions, this achieved rate can be compared to a theoretical upper bound.

IV. UPPER BOUND ON VRBC DATA RATE

To declare an upper bound on the possible communication rate, the data processing inequality is first used on the mutual information that is used in defining the mutual information rate

$$\mathcal{I}(m_q; \hat{m}_q) \leq \mathcal{I}(m_q; \mathbf{y}_q). \quad (36)$$

Therefore,

$$R \leq \frac{\mathcal{I}(m_q; \mathbf{y}_q)}{T_{\text{sym}}} = \frac{h(\mathbf{y}_q) - h(\mathbf{y}_q|m_q)}{T_{\text{sym}}}, \quad (37)$$

where $h(\cdot)$ now indicates differential entropy.

The differential entropy of the output signal data vector is

$$h(\mathbf{y}_q) = - \int f(\mathbf{y}_q) \log_2 f(\mathbf{y}_q) d\mathbf{y}_q. \quad (38)$$

Recall that Equation 28 shows that the distribution of the output data vector is a homoscedastic (same covariance) complex multivariate Gaussian mixture. Unfortunately, there is no analytical solution to the differential entropy of a complex multivariate Gaussian homoscedastic mixture. An upper bound on this differential entropy is found by using the lower bound for the expected value of log-sum [26]. The resultant differential entropy is

$$h(\mathbf{y}_q) \leq - \sum_{s=1}^S \sum_{m \in \mathcal{M}^{(s)}} \pi_{s,m} \log_2(\zeta_{s,m}) + h(\mathbf{y}_q|s_q, m_q) \quad (39)$$

where

$$\zeta_{s,m} = \sum_{s'=1}^S \sum_{m' \in \mathcal{M}^{(s')}} \pi_{s',m'} 2^{-\beta_{m,s,m',s'}},$$

$$\beta_{m,s,m',s'} = \left(\mathbf{a}^{(s,m)} - \mathbf{a}^{(s',m')} \right)^H \Gamma^{-1} \left(\mathbf{a}^{(s,m)} - \mathbf{a}^{(s',m')} \right),$$

and shorthand

$$\pi_{s,m} = \Pr(s_q = s, m_q = m).$$

Proof: The inequality used in proving this upper bound on differential entropy is the lower bound on the expected value of a log-sum, $\mathbb{E}_g[\log_2 \sum_k f(x_k)] \geq \log_2 \sum_k 2^{\mathbb{E}_g[\log_2 f(x_k)]}$. Appendix B provides a more detailed proof of this inequality.

Note that the distribution of \mathbf{y}_q can be considered a single Gaussian mixture even though it is distinctly written as a a mixture of mixtures. Let \mathcal{W} and w represent the set that the

double summations span and variable that represents a state and current symbol combination respectively. The Kullback-Liebler (KL) distance between two homoscedastic complex multivariate Gaussians distributions can be written as

$$\text{KL}(f(\mathbf{y}_q|w_q = w) || f(\mathbf{y}_q|w_q = w')) = \beta_{w,w'}. \quad (40)$$

Using shorthand for a conditional distribution $f(\mathbf{y}_q|w_q = w)$ as f_w , conditional differential entropy $h(\mathbf{y}_q|w_q = w)$ as h_w , KL distance $\text{KL}(f(\mathbf{y}_q|w_q = w) || f(\mathbf{y}_q|w_q = w'))$ as $\text{KL}(w || w')$, and probability $\Pr(w_q = w)$ as π_w ,

$$\begin{aligned} h(\mathbf{y}_q) &= - \int \sum_{w \in \mathcal{W}} \pi_w f_w \log_2 \left(\sum_{w' \in \mathcal{W}} \pi_{w'} f_{w'} \right) d\mathbf{y}_q \\ &= - \sum_{w \in \mathcal{W}} \pi_w \mathbb{E}_{f_w} \left[\log_2 \left(\sum_{w' \in \mathcal{W}} \pi_{w'} f_{w'} \right) \right] \\ &\leq - \sum_{w \in \mathcal{W}} \pi_w \log_2 \left(\sum_{w' \in \mathcal{W}} 2^{\mathbb{E}_{f_w}[\log_2 \pi_{w'} f_{w'}]} \right) \\ &= - \sum_{w \in \mathcal{W}} \pi_w \log_2 \left(\sum_{w' \in \mathcal{W}} 2^{\int f_w \log_2 \frac{\pi_{w'} f_{w'}}{f_w} d\mathbf{y}_q} \right) \\ &= - \sum_{w \in \mathcal{W}} \pi_w \log_2 \left(\sum_{w' \in \mathcal{W}} \pi_{w'} 2^{-h_w} 2^{-\text{KL}(w || w')} \right) \\ &= \sum_{w \in \mathcal{W}} \pi_w h_w - \sum_{w \in \mathcal{W}} \pi_w \log_2 \left(\sum_{w' \in \mathcal{W}} \pi_{w'} 2^{-\beta_{w,w'}} \right). \end{aligned} \quad (41)$$

Rewriting Equation 41 without the shorthand notation gives Equation 39. ■

Because $h(\mathbf{y}_q|m_q) \geq h(\mathbf{y}_q|s_q, m_q)$, substituting the bound on $h(\mathbf{y}_q)$ into the equation for rate provides the upper bound

$$R_{\text{KL UB}} = - \sum_{s=1}^S \sum_{m \in \mathcal{M}^{(s)}} \frac{\pi_{s,m}}{T_{\text{sym}}} \log_2(\zeta_{s,m}). \quad (42)$$

Alternatively, because the complex multivariate Gaussian mixture considered in bounding the differential entropy is homoscedastic, the basic upper bound used in [27] reduces to the simple bound provided by the entropy of M -ary communications,

$$R_{M\text{-ary UB}} = - \sum_{m=1}^M \frac{\Pr(m_q = m)}{T_{\text{sym}}} \log_2 \Pr(m_q = m). \quad (43)$$

As SNR increases, it is seen that the exponential in Equation 42 goes to 0 and the bound on the rate increases to equate to M -ary communications bound if the number of state and current symbol combinations is equivalently the number of symbols. This will lead to a less tight bound than $R_{M\text{-ary UB}}$ otherwise. For this reason, our full upper bound is written as

$$R_{\text{UB}} = \min\{R_{\text{KL UB}}, R_{M\text{-ary UB}}\}. \quad (44)$$

For all cases, higher SNR will lead to using the M -ary upper bound over the KL-derived bound, but at what SNR this occurs is entirely dependent on the excitations used and transponder impulse response. Regardless, once this M -ary upper bound is reached in VRBC, the only ways rate can be increased is

by increasing the number of symbols used, decreasing the symbol length, or better balancing the probabilities of the different symbols if they are not already equiprobable which may require better choices in the symbol excitations such that the multiple symbol data vectors are more orthogonal.

V. VRBC SIMULATION RESULTS

In this section, we continue to use the scenario in which $M = 3$ to demonstrate key discussion points of VRBC operation. In practice, the choice of M should be made with the transponder's expected impulse response in mind. A larger M naturally provides potential for a higher rate, but a given transponder will likely only have a handful of resonant frequencies that will result in an adequate amount of displacement. We use a PRF = 4 kHz, symbol length of $T_{\text{sym}} = 5$ ms, ADC sampling frequency of 1 MHz, and therefore an $L_{\text{sym}} = 5000$. An arbitrary single set of $M = 3$ frequency shift-keying symbol excitations are considered. They consist each of a tone at 800, 600, and 400 Hz respectively.

Signal to noise ratio (SNR) is defined here as the ratio of the variance of the target return gain/attenuation term, $\tilde{\alpha}_{\text{tar}}$, to the variance of the AWGN noise,

$$\text{SNR} = \frac{\mathbb{E}[|\tilde{\alpha}_{\text{tar}}|^2]}{\sigma_n^2}. \quad (45)$$

As an example, consider a radar whose peak receiver gain is ≈ 48 dB, transmit power is 12 dBm, system loss is 8 dB, and noise figure is ≈ 15 dB (resulting in thermal noise of about 0.65 pW), keeping in mind that atmospheric loss ≈ 0.2 dB/km, and considering a 6 in. (0.15 m) \times 12 in. (0.3 m) fully reflective license plate transponder surface, these SNRs relate to transponder range via

$$\text{SNR} \approx \frac{(0.15^2)(0.3^2)}{(4\pi r_{\text{obj}}^2)^2} 10^{(13.4 - 0.00002 r_{\text{obj}})}. \quad (46)$$

This relationship was calculated using Equation 47 and recognizing that $\sigma_{\text{obj}} = 4\pi h^2 w^2 / \lambda^2$ for a fully reflective $h \times w$ plate. This means that for this example radar/transponder scenario that SNRs of $[-10, -5, 0, 5, 10]$ dB correspond to ranges of $[238, 179, 133, 100, 75]$ meters. Naturally, these are maximum SNRs assuming the rectangular transponder's surface is perfectly perpendicular to the radar's main beam. If instead of a license plate, a trihedral corner reflector were used to make the transponder's SNR less dependent on angular orientation, the same SNR could be achieved when the corner reflector's edge length, l , is approximately 0.28 m, $\sigma_{\text{obj}} = \frac{4\pi l^4}{3\lambda^2}$.

Throughout this section we show Monte Carlo results for the communication rate compared to the theoretical upper bound (blue). The simulated experimental results include when the detection methods used are symbol maximum likelihood detection (yellow), and the Viterbi algorithm on the states (teal). 100 iterations of 50-length sequences were used at each SNR for Monte Carlo results.

In the following subsections, we discuss how to decide between single symbol and sequence detection methods depending on the transponder's impulse response and the coding constraint used.

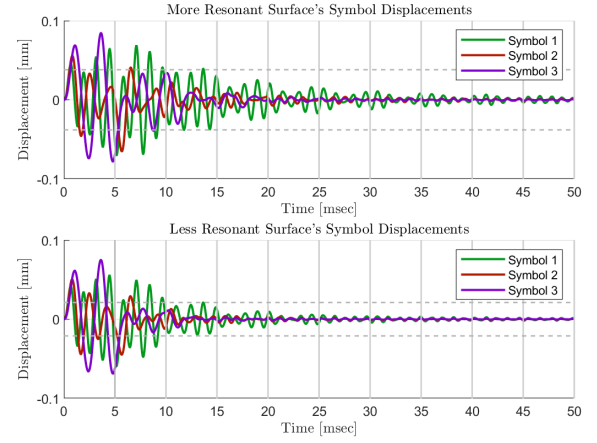


Fig. 4. The displacements used to compare the detection methods between two levels of resonance. Solid gray vertical lines indicate symbol interval boundaries, while dashed gray horizontal lines indicate the transponder's γ_{min} boundaries.

A. Choosing a Detection Method Based on a Transponder's Level of Resonance

Consider two impulse responses consisting of a sum of decaying sinusoids at resonant frequencies measured from an aluminum plate. The impulse responses differ only in the decay factor of the various resonant frequencies to demonstrate the importance of recognizing the degree of resonance present in a VRBC surface of interest when choosing what detection method should be used. The first impulse response corresponds to the surface that is more resonant and therefore contains the most ISI. The second is less resonant. Fig. 4 shows the symbol displacements over multiple symbol intervals for the two scenarios. Due to the variation in resonances, γ_{min} is adjusted such that system's symbol-specific resonances come out to $\mathcal{N} = \{2, 1, 1\}$ for both cases. This allows the comparison between these two cases to highlight when sequence versus symbol detection is preferable.

For the more resonant surface, a $\gamma_{\text{min}} = 0.45$ is used (solid). In other words, the requirement for considering ISI negligible is relatively relaxed. For the second case, $\gamma_{\text{min}} = 0.25$ (dashed). A no-consecutive symbol coding constraint is used for both cases. Fig. 5 shows the surfaces' resultant communication rates.

These two examples demonstrate that the added complexity of implementing sequence detection does not always lead to a significant increase in performance. According to Fig. 5, when the transponder is more resonant, the Viterbi algorithm does prove to increase the rate achieved significantly. Fig. 5 also shows that sequence detection can provide a slight increase in performance for a less resonant transponder. As shown in Section III, sequence detection comes at the cost of additional modeling and computational power, which may in turn make sequence detection undesirable for less resonant surfaces. Though not shown, it is possible to inaccurately model ISI like setting γ_{min} such that one symbol barely requires an additional interval to decay while the others barely do not. Doing so can lead to worse sequence detection performance as

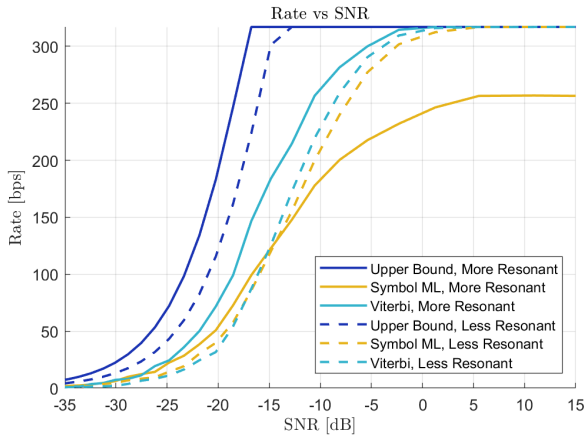


Fig. 5. Upper bound and simulated communication rates for the more resonant transponder (solid) and less resonant (dashed) when $\mathcal{N} = \{2, 1, 1\}$ and a no-consecutive symbols constraint is utilized.

it results in invoking inaccurate symbol interval dependencies. For this reason, we focus on cases where ISI modeling utilizes a significant γ_{\min} , ie. greater than about 0.1, and we have checked that the symbol displacements do not appear to provide borderline ISI requirements.

One final observation from the results of transponders at different levels of resonance is that ISI can cause the M -ary upper bound to be unachievable by either detection methods. Though we only show a case for single symbol detection not achieving the upper bound the same reasoning could apply to sequence detection if ISI is inaccurately modeled. For the more resonant surface's single symbol detection results, ISI is so great that certain sequences will always result in incorrect detections even when there is no noise present, see the solid yellow line in Fig. 5. These cases can be understood by considering when a previous symbol provides larger enough interference that it will mask the current symbol. In trying to design VRBC systems that achieve the M -ary upper bound at high SNRs, symbol-specific data vectors must be made orthogonal and have similar decay rates.

B. Choosing a Detection Method Based on Imposed Communication Message Constraints

We now consider how coding constraints affect our choice in detection method. Thus far, we have adopted the no-consecutive symbol constraint. We now vary this and consider coding constraints that are based on the resonances of the VRBC transponder. In aiming to align a coding constraint with the characteristics of the system, begin by considering the less resonant surface we just presented where $\mathcal{N} = \{2, 1, 1\}$. Now, require symbols to be separated in accordance with \mathcal{N} . In other words, consecutive m -symbols must have at least $N^{(m)}$ intervals between them (solid). We also consider if this was relaxed to $N^{(m)} - 1$ intervals between consecutive symbols (dashed). Simulating a coding constraint that is more restrictive than \mathcal{N} , such as requiring $N^{(m)} + 1$ intervals between consecutive symbols, is not possible in this case. It would lead to the set of available symbols at certain intervals

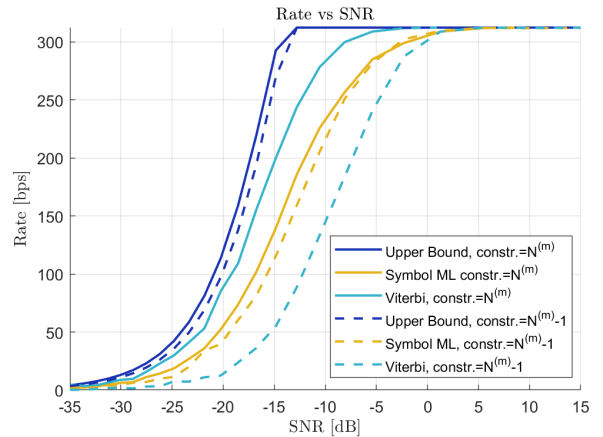


Fig. 6. Upper bound and simulated communication rates for the less resonant transponder where $\mathcal{N} = \{2, 1, 1\}$ and the coding constraint used requires either $N^{(m)}$ intervals (solid) or $N^{(m)} - 1$ intervals (dashed) between consecutive symbols.

being empty due to the need for previous symbols to decay further before reuse. Fig. 6 shows the results for the two coding constraints described.

Since the ultimate goal of communication systems is to achieve larger rates, we find that the best performance coincides with having coding constraints and ISI modeling align. This can be seen as when the $N^{(m)}$ constraint is used in combination with sequence detection. Fig. 5 also shows that when modeling ISI to a larger degree than what the coding constraint is handling, like in the $N^{(m)} - 1$ constraint, single symbol detection can become a better choice for detection. To achieve rates closer to the upper bound in VRBC, we therefore recommend aligning line coding constraints with the resonances of the surface in order to benefit most from sequence detection.

VI. CONCLUSION

In this paper, we provided a model, processing chain, and rate upper bound for VRBC, which serves as a backscatter communication solution at mmW. We discussed different VRBC scenarios in order to demonstrate when modeling ISI and using sequence detection allows VRBC to achieve data rates closer to its upper bound. These scenarios included variations in transponder resonance as well as coding constraints. Selection of in symbol set cardinality and pulse repetition frequency were left unexplored, though these naturally affect communication rates as well. Different choices in symbol excitation waveform can also provide higher rates when they result in data vectors, \mathbf{a}_q , that are closer to orthogonal [8]. We provided the methodology necessary for performing single symbol and sequence maximum likelihood detection in any case, though future work should explore optimal transponder design, radar parameter choices, and messaging choices.

For application in anything-to-vehicle communications, the additional consideration of background vibrations such as that of a vehicle must be considered. VRBC displacement frequencies need to be distinctly recognizable in the presence

of such noise. Either prior automotive noise knowledge or real-time noise estimation methods are required to design VRBC symbols such that they provide sufficient SNR in Doppler. This along with improvements in transponder design to allow for a larger number of symbols (larger M) and adequate return from multiple incident angle describe a few areas of future work in VRBC.

APPENDIX A RETURN POWER CALCULATIONS USING THE RADAR EQUATION

The object-specific attenuation terms, $\tilde{\alpha}_{\text{obj}}$, have a phase drawn from a uniform distribution and magnitude drawn from a Rayleigh distribution in accordance with the Swerling model. Furthermore, they are zero-mean with a variance calculable via the radar range equation,

$$\mathbb{E}[|\tilde{\alpha}_{\text{obj}}|^2] = \underbrace{\left(\frac{G_{\text{TX}}}{4\pi r_{\text{obj}}^2}\right)}_{\text{ratio of TX power incident upon the object}} \underbrace{\left(\frac{\sigma_{\text{obj}}}{4\pi r_{\text{obj}}^2}\right)}_{\text{ratio of the power reflected back to the radar}} \underbrace{\left(\frac{1}{L_s L_a(r_{\text{obj}})}\right)}_{\text{losses due to the system and atmosphere}} \underbrace{A_{\text{eff}}}_{\text{effective aperture size of antenna(s)}}. \quad (47)$$

G_{TX} is the transmission gain, σ_{obj} is the radar cross section of the object, and L_s is the loss in linear units due to the system. $L_a(r_{\text{obj}})$ is the loss in linear units due to the atmosphere,

$$L_a(r_{\text{obj}}) = 10^{\kappa r_{\text{obj}}/5000}, \quad (48)$$

where κ is the loss in decibels per kilometer due to the atmosphere. A_{eff} is the effective aperture size of the receiving antenna(s) which is a function of the gain from the receive antenna(s), G_{RX} , and the operating wavelength, $\lambda_0 = c/f_0$. The general relation for the effective aperture in terms of the receive antenna gain is given by

$$A_{\text{eff}} = \frac{\lambda_0^2}{4\pi} G_{\text{RX}}. \quad (49)$$

These attenuation terms are modeled as such because a given scatterer is assumed to contain multiple reflecting surfaces. The Central Limit Theorem allows the separate effects from each surface to be approximated into an inclusive single Gaussian term with the statistical properties described.

APPENDIX B LOWER BOUND ON EXPECTATION OF LOG-SUM

Because \log_2 is a concave function, we know

$$\log_2 \left(\sum_k \pi_k x_k \right) \geq \sum_k \pi_k \log_2 x_k, \quad (50)$$

where $\pi_k \geq 0$ for all k , $\sum_k \pi_k = 1$, and x_k is an arbitrary random variable that takes on some distribution according to k . Specifically, we choose $\pi_k = \frac{2^{\mathbb{E}_g[\log_2 f(x_k)]}}{\sum_l 2^{\mathbb{E}_g[\log_2 f(x_l)]}}$. This choice in π_k is not arbitrary. The achieve a tight lower bound and can be solved for using Lagrange multipliers to choose the set of π_k that maximize the lower bound while still requiring that

they sum to 1. The expectation used in this proof is taken over a distribution notated g . Therefore,

$$\begin{aligned} \mathbb{E}_g \left[\log_2 \sum_k f(x_k) \right] &= \mathbb{E}_g \left[\log_2 \sum_k \frac{\pi_k f(x_k)}{\pi_k} \right] \\ &\geq \mathbb{E}_g \left[\sum_k \pi_k \log_2 \left(\frac{f(x_k)}{\pi_k} \right) \right] \\ &= \sum_k \pi_k \mathbb{E}_g \left[\log_2 \left(\frac{f(x_k)}{\pi_k} \right) \right] \\ &= \sum_k \pi_k (\mathbb{E}_g [\log_2 f(x_k)] - \log_2 \pi_k) \\ &= \sum_k \pi_k \left(\log_2 2^{\mathbb{E}_g[\log_2 f(x_k)]} - \log_2 \pi_k \right) \\ &= \sum_k \pi_k \log_2 \frac{2^{\mathbb{E}_g[\log_2 f(x_k)]}}{\pi_k} \\ &= \sum_k \pi_k \log_2 \sum_l 2^{\mathbb{E}_g[\log_2 f(x_l)]} \\ &= \log_2 \sum_l 2^{\mathbb{E}_g[\log_2 f(x_l)]}. \end{aligned} \quad (51)$$

To summarize, the lower bound on the expectation of a log-sum is

$$\mathbb{E}_g \left[\log_2 \sum_k f(x_k) \right] \geq \log_2 \sum_k 2^{\mathbb{E}_g[\log_2 f(x_k)]}. \quad (52)$$

REFERENCES

- [1] H. Stockman, "Communication by Means of Reflected Power," in Proceedings of the IRE, vol. 36, no. 10, pp. 1196-1204, Oct. 1948, doi: 10.1109/JRPROC.1948.226245.
- [2] F. Guidi, N. Decarli, D. Dardari, F. Mani and R. D'Errico, "Passive Millimeter-Wave RFID Using Backscattered Signals," IEEE Globecom Workshops (GC Wkshps), pp. 1-6, 2016, doi: 10.1109/GLOCOMW.2016.7848994.
- [3] F. Boccardi, R. W. Heath, A. Lozano, T. L. Marzetta and P. Popovski, "Five disruptive technology directions for 5G," in IEEE Communications Magazine, vol. 52, no. 2, pp. 74-80, February 2014, doi: 10.1109/MCOM.2014.6736746.
- [4] J. Niu and G. Y. Li, "An Overview on Backscatter Communications," Journal of Communications and Information Networks, vol. 4, no. 2, pp. 1-14, June 2019, doi: 10.23919/JCIN.2019.8917868.
- [5] J. Kimionis, A. Georgiadis and M. M. Tentzeris, "Millimeter-wave backscatter: A quantum leap for gigabit communication, RF sensing, and wearables," 2017 IEEE MTT-S International Microwave Symposium (IMS), 2017, pp. 812-815, doi: 10.1109/MWSYM.2017.8058702.
- [6] M. Alhassoun, "Theory and Design of Next-Generation Retrodirective Tags and Their Channels," PhD. Dissertation, Georgia Institute of Technology, Dec. 2019.
- [7] E. Soltanaghaei, A. Prabhakara, A. Balanuta, M. Anderson, J. M. Rabaey, S. Kumar, and A. Rowe, "Millimetro: mmWave retro-reflective tags for accurate, long range localization," Proceedings of the 27th Annual International Conference on Mobile Computing and Networking (MobiCom '21), Association for Computing Machinery, 2021, doi:https://doi.org/10.1145/3447993.3448627.
- [8] J. Centers and J. Krolik, "Vibrational Radar Backscatter Communications," 2021 55th Asilomar Conference on Signals, Systems, and Computers, 2021, pp. 1086-1090.
- [9] S. Bakhtiari, N. Gopalsami, T. W. Elmer, and A. C. Raptis, "Millimeter wave sensor for far-field standoff vibrometry," AIP Conference Proceedings, vol. 1096, no. 1, pp. 1641-1648, 2009.
- [10] C. T. Rodenbeck, J. B. Beun, R. G. Raj and R. D. Lipps, "Vibrometry and Sound Reproduction of Acoustic Sources on Moving Platforms Using Millimeter Wave Pulse-Doppler Radar," IEEE Access, vol. 8, pp. 27676-27686, 2020, doi: 10.1109/ACCESS.2020.2971522

- [11] F. Tonolini and F. Adib, "Networking across Boundaries: Enabling Wireless Communication through the Water-Air Interface," *ACM SIGCOMM* 2018, 2018, doi:10.1145/3230543.3230580
- [12] N. T. P. Van, L. Tang, V. Demir, S. F. Hasan, N. D. Minh, and S. Mukhopadhyay, "Review-microwave radar sensing systems for search and rescue purposes," *Sensors*, vol. 19, no. 13, p. 2879, Jun. 2019.
- [13] Huining Li, Chenhan Xu, Aditya Singh Rathore, Zhengxiong Li, Hanbin Zhang, Chen Song, Kun Wang, Lu Su, Feng Lin, Kui Ren, and Wenyao Xu. 2020. VocalPrint: exploring a resilient and secure voice authentication via mmWave biometric interrogation. *Proceedings of the 18th Conference on Embedded Networked Sensor Systems*. Association for Computing Machinery, New York, NY, USA, 312–325. <https://doi.org/10.1145/3384419.3430779>
- [14] T. Yucek and H. Arslan, "A survey of spectrum sensing algorithms for cognitive radio applications," *IEEE Communications Surveys and Tutorials*, vol. 11, no. 1, pp. 116-130, First Quarter 2009, doi: 10.1109/SURV.2009.090109.
- [15] N. C. Luong, X. Lu, D. T. Hoang, D. Niyato and D. I. Kim, "Radio Resource Management in Joint Radar and Communication: A Comprehensive Survey," *IEEE Communications Surveys and Tutorials*, vol. 23, no. 2, pp. 780-814, Secondquarter 2021, doi: 10.1109/COMST.2021.3070399.
- [16] M. Labib, V. Marojevic, A. F. Martone, J. H. Reed, and A. I. Zaghloul, "Coexistence between communications and radar systems: A survey," *URSI Radio Sci. Bull.*, vol. 2017, no. 362, pp. 74–82, Sep. 2017.
- [17] A. R. Chiriyath, B. Paul, G. M. Jacyna, and D. W. Bliss, "Inner bounds on performance of radar and communications co-existence," *IEEE Trans. Signal Process.*, vol. 64, no. 2, pp. 464–474, Jan. 2016.
- [18] J. Jakabosky, B. Ravenscroft, S. D. Blunt, and A. F. Martone, "Gapped spectrum shaping for tandem-hopped radar/communications and cognitive sensing," *Proc. IEEE Radar Conf.*, Philadelphia, PA, USA, May 2016, pp. 1–6.
- [19] N. Cao, Y. Chen, X. Gu and W. Feng, "Joint Radar-Communication Waveform Designs Using Signals From Multiplexed Users," *IEEE Transactions on Communications*, vol. 68, no. 8, pp. 5216-5227, Aug. 2020, doi: 10.1109/TCOMM.2020.2994215.
- [20] M. Robertson and E. Brown, "Integrated radar and communications based on chirped spread-spectrum techniques," *IEEE International Microwave Symposium Digest*, vol. 1, 2003, pp. 611–614.
- [21] C. Sahin, J. Jakabosky, P. M. McCormick, J. G. Metcalf, and S. D. Blunt, "A novel approach for embedding communication symbols into physical radar waveforms," *2017 IEEE Radar Conference (RadarConf)*. IEEE, 2017, pp. 1498–1503.
- [22] R. Molina-Masegosa, J. Gosalvez and M. Sepulcre, "Comparison of IEEE 802.11p and LTE-V2X: An Evaluation With Periodic and Aperiodic Messages of Constant and Variable Size," in *IEEE Access*, vol. 8, pp. 121526-121548, 2020, doi: 10.1109/ACCESS.2020.3007115.
- [23] C. Li, N. Raymondi, B. Xia and A. Sabharwal, "Outer Bounds for a Joint Communicating Radar (Comm-Radar): The Uplink Case," in *IEEE Transactions on Communications*, vol. 70, no. 2, pp. 1197-1213, Feb. 2022, doi: 10.1109/TCOMM.2021.3126741.
- [24] M. A. Richards, "Fundamentals of Radar Signal Processing," McGraw-Hill Companies, Inc., 2005.
- [25] J. Yu and J. Krolik, "MIMO multipath clutter mitigation for GMTI automotive radar in urban environments," *IET International Conference on Radar Systems (Radar 2012)*, pp. 1-5, 2012. doi: 10.1049/cp.2012.1565.
- [26] A. Kolchinsky and B. D. Tracey, "Estimating Mixture Entropy with Pairwise Distances," *MDPI Entropy Journal*, vol. 19 (7), no. 361, July 2017. doi: 10.3390/e19070361.
- [27] M. F. Huber, T. Bailey, H. Durrant-Whyte and U. D. Hanebeck, "On entropy approximation for Gaussian mixture random vectors," *2008 IEEE International Conference on Multisensor Fusion and Integration for Intelligent Systems*, 2008, pp. 181-188, doi: 10.1109/MFI.2008.4648062.
- [28] J. Centers and J. Krolik, "Vibrational Radar Backscatter Communication using Resonant Transponding Surfaces," *2022 IEEE 12th Sensor Array and Multichannel Signal Processing Workshop (SAM)*, 2022, pp. 71-75
- [29] I. Cnaan-On, S. J. Thomas, J. L. Krolik and M. S. Reynolds, "Multichannel Backscatter Communication and Ranging for Distributed Sensing With an FMCW Radar," *IEEE Transactions on Microwave Theory and Techniques*, vol. 63, no. 7, pp. 2375-2383, July 2015. doi: 10.1109/TMTT.2015.2439678.
- [30] T. M. Cover and J. A. Thomas, "Elements of Information Theory, 2nd Edition," New York: John Wiley & Sons, 2006.
- [31] H. L. Van Trees, K. L. Bell, Z. Tian, "Detection, Estimation, and Modulation Theory: Part I Detection, Estimation, and Filtering Theory, 2nd Edition," Wiley-Interscience, 2013.

Jessica Centers (Student Member, IEEE) is a Ph.D. candidate in the Electrical and Computer Engineering Department at Duke University focusing in signal and information processing. She received her B.S. in Electrical Engineering from Milwaukee School of Engineering in 2018. Her current research interests include signal processing, communication systems, physics-motivated machine learning, engineering education, and technology ethics and policy. At Duke, she has been a 2021–2022 Bass Digital Education Fellow and spring 2022 Teaching with Purpose Fellow.

Jeffrey Krolik (Senior Member, IEEE) is Professor of Electrical and Computer Engineering at Duke University in Durham, NC. Canadian-born, he received his Ph.D. in Electrical Engineering from the University of Toronto in 1987. He held academic positions at Concordia University in Montreal and the University of California San Diego before coming to Duke in 1992. In 2008, he founded STRAD Corporation, a Duke spin-off performing classified research in sonar, radar, and electronic warfare. From December 2014 until August 2019, he served as a Program Manager in the DARPA Strategic Technology Office (STO) conceiving and managing several radar programs, including the Space-based HF Testbed, and Aerial Dragnet, a counter-unmanned aerial systems program. His groups at Duke and STRAD are supported by ONR, DARPA, and AFRL. He also serves as the Managing Director of the Athena seven-university NSF AI Institute for Edge Computing lead by Duke. He is a Fellow of the IEEE and was a founding member of the Sensor and Multichannel Signal Processing Technical Committee of the IEEE Signal Processing Society.